ICAS 2021 SHANGHAI
32nd Congress of the International Council of the Aeronautical Sciences
September 6-10, 2021 Pudong Shangri-La, Shanghai, China

HYBRID NUMERICAL SCHEMES IN PREDICTION OF HIGH-SPEED LAMINAR-TURBULENT TRANSITION

I. V. Egorov[1,2], A.V. Novikov[1,2], N.K. Nguen[1]

[1] Moscow Institute of Physics and Technology
[2] Central Aerohydrodynamic Institute

Abstract

A simple hybrid difference scheme is proposed which is applicable in shock wave flows. The scheme remains monotonic near shock waves and switches to a low-dissipative, non-monotonic difference scheme in smooth flow regions, adjusting the amount of numerical dissipation. This is achieved by smoothly reducing the monotonic correction to a given threshold level depending on the solution smoothness indicator. As an example, we consider the problem of modeling the laminar-turbulent transition in the supersonic boundary layer over a flat plate at Mach number 3. Computational results are compared with results of other works in which both dissipative and low dissipative schemes were applied. The spectral characteristics of disturbances in the region of their linear and nonlinear development as well as the structure of a transient flow and characteristics of the averaged boundary layer are compared.

Keywords: hybrid scheme, monotonic scheme, low-dissipative scheme, numerical simulation, laminar-turbulent transition.

1. Introduction

The development of promising aircraft includes a detailed study of streamlined aerodynamic shapes. The experimental part is usually associated not only with the financial costs of staging and conducting the wind tunnel experiment, but also with the limited information obtained in the experiment. The numerical simulation of the non-stationary motion of compressible gas allows us to describe the flow near the bodies of arbitrary configuration, to reveal the fine structure of the phenomena considered and get the results, which are difficult to obtain by experimental means. The aerothermodynamic coefficients - pressure, friction and heat transfer coefficients - are calculated from the results of modelling. The latter become critical in the case of high supersonic and hypersonic flow velocities, especially when flow turbulence occurs and with it friction and heat transfer coefficients to the surface increase several times.

Pipe test data for the laminar-turbulent transition (LTT) problem is not constant, as it depends on the background of the flow disturbance in a particular wind tunnel. In view of this, the results of direct numerical simulation of flows in the laminar-turbulent transition regime, when such background can be strictly controlled, are of particular value. Unfortunately, the spatial and temporal costs for such simulations are high for regimes close to the practically important one. The use of high-performance multiprocessor computer clusters (supercomputers) allows only single calculations, the purpose of which is to investigate linear and nonlinear mechanisms underlying LTT.

Increasing the accuracy of the computational schemes used helps to reduce the requirements for spatial resolution of the flow, when it is the stage of LTT and the initial section of turbulence motion ("young" turbulence) that is directly modeled. However, increasing the accuracy destabilises the numerical algorithms, e.g. in the presence of strong shock waves. Therefore, the use of monotonic Godunov-type schemes may be justified. The monotonicity of the solution is achieved by considering discontinuous solutions based on the Riemann disintegration problem of an arbitrary discontinuity. In this case a monotonic correction is added to the approximation of convective flux terms which indirectly introduces additional dissipation and thus stabilizes the numerical solution in regions of strong discontinuities and suppresses small perturbations [1]. The latter can play a significant role in the LTT process.

This work is an extension of [1]: the possibility of reducing this kind of dissipation in areas where it is not necessary (e.g. inside a gradientless boundary layer) is investigated. The simulation results are compared with the results of paper [1] obtained using the dissipative scheme (described below)

and with the results of paper [2] obtained using the low dissipative method. In [2] the fourth order accuracy scheme in longitudinal and normal to the surface directions, as well as spectral method in the lateral direction were used. The time integration in [2] is done by the Runge-Kutta method of fourth order approximation.

2. Problem statement

2.1 Numerical method

In this paper we used a software package [3] for numerical integration of the full Navier-Stokes equations. Equations are solved in curvilinear coordinate system (ξ,η,ζ) in dimensionless divergent form

$$\frac{\partial \boldsymbol{Q}}{\partial t}+\frac{\partial \boldsymbol{E}}{\partial \xi}+\frac{\partial \boldsymbol{G}}{\partial \eta}+\frac{\partial \boldsymbol{F}}{\partial \zeta}=0.$$

The Cartesian coordinates $x^*=xL$, $y^*=yL$, $z^*=zL$ are referred to the characteristic length scale *L*, time $t^*=tL/V_\infty$ to the characteristic time scale L/V_∞, components of the velocity vector $u^*=uV_\infty$, $v^*=vV_\infty$, $w^*=wV_\infty$ - to the modulus of the velocity vector of the incoming flow V_∞, pressure $p^*=p(\rho_\infty V_\infty^2)$ - to the doubled velocity head in the incoming flow, the other gas-dynamic variables to their values in the incoming flow. The asterisk in the upper index indicates a dimensional value; if there is no asterisk, the variable is assumed to be dimensionless. The symbol " ∞ " denotes a reference to an incoming flow. Dimensional variables will be used for ease of comparison with the results of other work.

A fully implicit finite volume method and a second order time approximation scheme are used to approximate differential equations:

$$\frac{3\boldsymbol{Q}_{i,j,k}^{n+1}-4\boldsymbol{Q}_{i,j,k}^{n}+\boldsymbol{Q}_{i,j,k}^{n-1}}{\Delta t}+\frac{\boldsymbol{E}_{i+\frac{1}{2},j,k}^{n+1}-\boldsymbol{E}_{i-\frac{1}{2},j,k}^{n+1}}{h_\xi}+\frac{\boldsymbol{G}_{i,j+\frac{1}{2},k}^{n+1}-\boldsymbol{G}_{i,j-\frac{1}{2},k}^{n+1}}{h_\eta}+\frac{\boldsymbol{F}_{i,j,k+\frac{1}{2}}^{n+1}-\boldsymbol{F}_{i,j,k-\frac{1}{2}}^{n+1}}{h_\zeta}=\boldsymbol{0}.$$

When determining the convective flux values on grid cell faces, e.g. $\boldsymbol{E}_{i+1/2,j,k}^{n+1}$, the fluxes are split in directions. For each direction, a Jacobi matrix ($A=\partial \boldsymbol{E}/\partial \boldsymbol{Q}$ for the direction ξ) is defined which is diagonalised in the form $A=B\Lambda B^{-1}$, where B is the matrix made up of the right-hand eigenvectors, and Λ is the diagonal matrix of eigenvalues of the matrix A.

The convective component of the flux quantities ***E, G, F*** at the cell face is approximated using a Godunov type monotone scheme (indices *i, j, k, n* are omitted for readability):

$$\boldsymbol{E}_{i+\frac{1}{2}}=\frac{1}{2}\Big[\boldsymbol{E}(\boldsymbol{Q}_L)+\boldsymbol{E}(\boldsymbol{Q}_R)-\Phi\times B_{LR}\Lambda(\varphi(\lambda_{LR}))B_{LR}^{-1}(\boldsymbol{Q}_R-\boldsymbol{Q}_L)\Big],$$

where the lower indices L and R denote the values calculated on the right and left sides of the face in question using the values of the gas-dynamic variables reconstructed using the reconstruction procedure. For example, for face i + 1/2, the index L corresponds to cell i and the index R to cell i + 1. The lower index LR indicates the values calculated using the approximate Roe method for solving the Riemann problem. The modification of the eigenvalues $\varphi(\lambda)$ provides a physically correct entropy change at discontinuities. The reconstruction procedure by the WENO-3 method is used in the paper.

The function Φ determines the degree of non-monotonicity of the scheme and takes values between 0 and 1. For the original monotonic scheme $\Phi=1$. For the hybrid scheme in the computational domain $\Phi=\max(\Phi_0,\Psi)$, where Φ_0 is some constant, Ψ is the Jameson indicator function [4]:

$$\Psi=\frac{(divV)^2}{(divV)^2+(rotV)^2+\varepsilon},\varepsilon=10^{-20} \quad (1)$$

The value ε is chosen as a small positive number and eliminates the numerical singularity of division by zero in regions where $div\vec{V}$ and $rot\vec{V}$ both are zero. The value Ψ varies from 0 at $(divV)^2\ll(rotV)^2$ to 1 in the case of $(divV)^2\gg(rotV)^2$. In particular, in the boundary layer $\Psi\to 0$,

and in the vicinity of the shock waves $\Psi \to 1$.

A buffer region (Figure 1) with grid spacing is organised upstream of the output boundary to suppress disturbances. In this area, the monotonic scheme (Φ tends to one) is smoothly restored downstream according to the formula:

$$\Phi = \begin{cases} 1-(1-\max(\Phi_0,\Psi))*\left(1-\dfrac{i-is}{k}\right), & если\ is \le i \le is+k \\ 1, & если\ i > is+k \end{cases},$$

where i - longitudinal grid index, is - initial buffer zone index, k - constant. In the present paper the value of $k=3$.

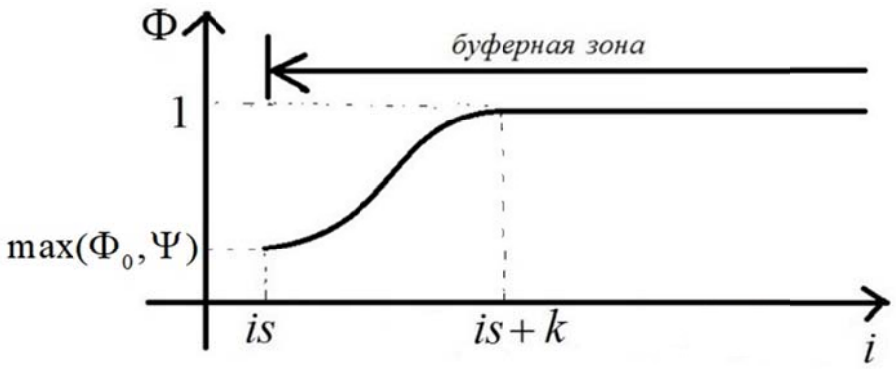

Figure 1 - Plot of the switch parameter of the dissipative component in the buffer zone for the case of hybrid scheme.

To approximate the diffusion component of the vectors ***E, G, F*** at the face of the unit cell, a second-order difference scheme of the central difference type is applied:

$$\left.\frac{\partial q}{\partial \xi}\right|_{i+\frac{1}{2},j,k} = \frac{1}{h_\xi}\left(q_{i+1,j,k}-q_{i,j,k}\right),$$

$$\left.\frac{\partial q}{\partial \eta}\right|_{i+\frac{1}{2},j,k} = \frac{1}{4h_\eta}\left(q_{i+1,j+1,k}+q_{i,j+1,k}-q_{i+1,j-1,k}-q_{i,j-1,k}\right),$$

$$\left.\frac{\partial q}{\partial \zeta}\right|_{i+\frac{1}{2},j,k} = \frac{1}{4h_\zeta}\left(q_{i+1,j,k+1}+q_{i,j,k+1}-q_{i+1,j,k-1}-q_{i,j,k-1}\right),$$

where q is any of the non-conservative ('primitive') dependent variables of the problem (u,v,w,p,T), the Cartesian components of velocity, pressure, temperature.

After approximation of Navier-Stokes equations and boundary conditions integration of initial equations in partial derivatives is reduced to solution of system of nonlinear algebraic equations $R(\boldsymbol{U})=0$, where R - discretization operator that calculates a vector of deviation according to approximation of equations, $\boldsymbol{U}$ - vector of unknown nonconservative variables (u,v,w,p,T) (velocity components, pressure, temperature) in all nodes of calculation grid. The vector $\boldsymbol{U}$ length is $n_q N$, where N is a total number of computational grid nodes including boundary nodes, n_q - number of unknowns in each node ($n_q = 5(u,v,w,p,T)$ in three-dimensional and $n_q = 4(u,v,p,T)$ in two-dimensional formulation). The system of mesh equations $R(\boldsymbol{U})=0$ is solved using modified Newton-Raphson method

$$\boldsymbol{U}^{[k+1]} = \boldsymbol{U}^{[k]} - \tau^{[k+1]}\left(J^{[k_0]}\right)^{-1} R\left(\boldsymbol{U}^{[k]}\right),$$

where k, k_0 are numbers of iterations on nonlinearity, $k_0 \le k$, $J^{[k_0]} = \left(\partial R/\partial \boldsymbol{U}\right)^{[k_0]}$ is Jacobi matrix of the system of nonlinear equations, $R(\boldsymbol{U}^{[k]})$ is a error vector, τ is regularization parameter. Here expression $\left(J^{[k_0]}\right)^{-1} R\left(\boldsymbol{U}^{[k]}\right) \equiv Y^{[k]}$ is solution of linear system of equations

$$\left(J^{[k_0]}\right)Y^{[k]} = R\left(\boldsymbol{U}^{[k]}\right).$$

The regularisation parameter of Newton's method with respect to the initial approximation $\tau^{[k]}$ is given by

$$\tau^{[\mathrm{k+1}]} = \frac{\left(Y^{[k]} - Y^{[\mathrm{k-1}]}\right)Y^{[k]}}{\left(Y^{[k]} - Y^{[k-1]}\right)^2}.$$

As the iterative process converges $\tau^{[k]} \to 1$, and the rate of convergence theoretically tends to be quadratic.

Obtaining the analytical form of the Jacobi matrix J for the numerical scheme in question, including the solution of the Riemann discontinuity problem, seems to be very time consuming. The package [3] applies a universal method of forming matrix $J^{[k_0]} = \left(\partial R / \partial \boldsymbol{U}\right)^{[k_0]}$ on iteration over nonlinearity k_0 using the procedure of finite increments of the error vector R over the vector of desired variables $\boldsymbol{U}$ [5]. In this case the m-th column of the matrix $J^{[k_0]}$ is calculated in the form

$$J_m^{[k_0]} = \frac{R\left(\boldsymbol{U}^{[k_0]} + \varepsilon \boldsymbol{e}_m\right) - R\left(\boldsymbol{U}^{[k_0]}\right)}{\varepsilon}, \varepsilon = 10^{-8}, m = 1,...,n_q N,$$

where $\boldsymbol{e}_m$ is a unit vector of length $n_q N$, consisting entirely of 0, except for a single 1 at position m. This Jacobian computation technique is applicable to an arbitrary system of mesh equations.

2.2 Flow parameters and calculation conditions

We consider a nominally two-dimensional flow over a pointed plane plate at Mach number of the incoming flow $M_\infty = 3$ and temperature of the incoming flow $T_\infty = 103.6\,\mathrm{K}$. The perturbation evolution is calculated in a subarea; the calculation procedure is similar to that described in [6]. The Reynolds number is $R_{1,\infty} = 2.181 \times 10^6$ m-1. The Prandtl number is assumed constant: $Pr = \mu c_p / \lambda = 0.71$. The Navier-Stokes equations are closed by the equation of state $\gamma M_\infty^2 p = \rho T$, where $\gamma = 1.4$ is the adiabatic exponent. The dynamic molecular viscosity coefficient is calculated using the Sutherland formula: $\mu = (1 + T_\mu) / (T + T_\mu) \times T^{3/2}$, where $T_\mu = T_\mu^* / T_\infty^* = 110.4K / 103.6K \approx 1.07$.

Numerical integration is carried out in the rectangular area shown below. At the inlet and upper boundary the dimensionless parameters of the incoming flow are fixed: $(u, v, w, p, T) = (1, 0, 0, 1/\gamma M_\infty^2, 1)$. For steady-state calculations the wall is assumed to be thermally insulated and sticking conditions are set on the wall. The outlet boundary is preceded by a buffer zone with enlarged cells for the longitudinal coordinate and the coordinate normal to the wall to damp the disturbances going out through the boundary. At the exit boundary, soft conditions are imposed as a linear extrapolation of the primitive variables from the computational domain. At the lateral boundaries $\mathrm{z}_{\min}$ and $\mathrm{z}_{\max}$ the symmetry conditions are imposed.

The calculation is carried out as follows. Firstly, a two dimensional steady state flow over a flat plate is computed until the unconvex value of 10^{-8} is reached. Second, the subarea in which further perturbation development will be simulated is cut out from the obtained solution; gas-dynamic values from the first step calculation are fixed at the new input boundaries of the subarea; the steady-state field is set additionally until full convergence (the magnitude of the misalignment does not exceed 10^{-8}). Third, the steady-state field obtained in the sub-area is duplicated in the third transverse direction z ; the surface temperature distribution is fixed; "blow-suction" perturbations are introduced into the boundary layer according to the procedure described below. The non-stationary calculation is carried out until a quasi-stationary flow regime is established. In this approach, the surface of the plate is adiabatic, but there are no temperature pulsations at the surface.

2.3 Jameson indicator function

The field of the Jameson indicator function [4] is calculated from a two-dimensional unperturbed flow and is shown in Figure 2. "Spotting" of this function value is related to numerical peculiarities of formula calculation (1).

For the calculations of this paper, the value Ψ is taken to be unity everywhere except in the vicinity of the boundary layer, where Ψ changes smoothly from 0 at the surface to 1 as one moves away from the boundary layer.

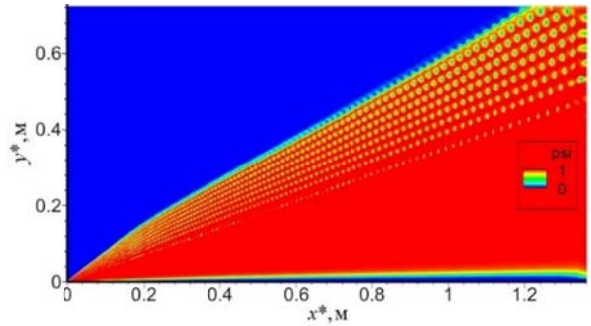

Figure 2 - Jameson function Ψ field .

Figure 3 shows the profiles $u(y)$ and $\Psi(y)$. It should be noted that the region $\Psi \ll 1$ occupies about two to three thicknesses of the unperturbed boundary layer. Therefore, at the initial stage of flow turbulization, the boundary layer continues to be in the region where a low-dissipative central difference type scheme is used to approximate the convective components of the flow quantities. In non-stationary calculations, the shape of the profiles $\Psi(y)$ is fixed at all cross sections $x = const$ and does not depend on the current perturbed flow field.

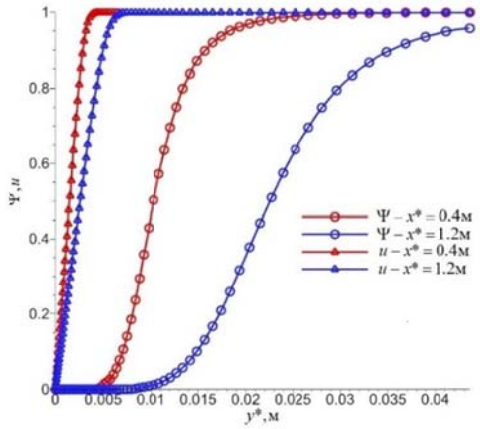

Figure 3 - Velocity and Jameson function profiles.

2.4 Determining the value Φ_0

With the described approach it is not possible to switch completely to a central difference scheme ($\Phi_0 = 0$), as the turbulence of the current shows numerical instability and the calculation process does not converge any more. Empirically it is possible to determine the smallest possible value Φ_0, at which the numerical integration of the differential equations remains stable. This value depends on the quality of the mesh and on perturbations. On a grid of 20 million nodes $\Phi_{0,\min} = 0.35$, and on a grid of 80 million nodes - $\Phi_{0,\min} = 0.21$.

Figure 4 shows the isosurfaces of the Q -criterion obtained on a coarse grid of 5 million nodes at points in time when the solution no longer converges. As can be seen, in all cases perturbations do not have time to reach the end of the computational domain, and the less dissipative the scheme is (the smaller the value of Φ_0), the earlier the computational problems appear. On the considered coarse grid $\Phi_{0,\min} = 0.3$, however, in this case the amplitude of the generated perturbations $\varepsilon = 0.003$. Below in this paper, as in [1], we consider the case of $\varepsilon = 0.00573$.

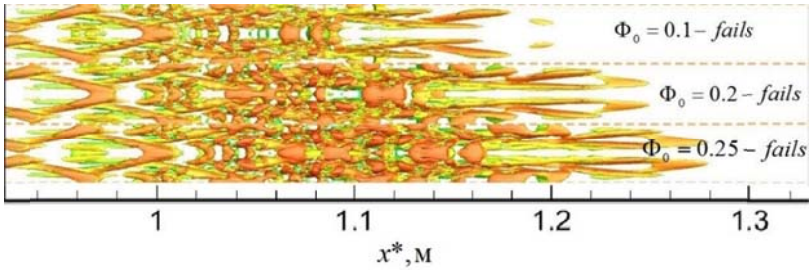

Figure 4 - Solution breakdowns, Q-criterion=15, top view, grid of 5 million nodes.

2.5 Perturbation generator

Perturbations are introduced into the boundary layer by means of an blowing-suction generator from the plate surface. The generator is modelled at $x^* \in [x_1^*, x_2^*] = [0.394, 0.452]$ m according to [1, 2]. In this range the normal component of the velocity vector is

$$v(x, y = 0, t) = A(t) v_p(x_p) \cos(\beta_0 z) \cos(-\omega_0 t),$$

where $v_p = \begin{cases} 1.5^4 (1 + x_p)^3 (3(1 + x_p)^2 - 7(1 + x_p) + 4), & -1 \le x_p \le 0 \\ -1.5^4 (1 - x_p)^3 (3(1 - x_p)^2 - 7(1 - x_p) + 4), & 0 \le x_p \le 1 \end{cases}$, $x_p = \dfrac{2x - (x_2 + x_1)}{x_2 - x_1}$,

$$A(t) = \varepsilon \begin{cases} 0 & , \quad t < 0, \\ 0.1^{((T-t)/(0.9T))^2} & , \quad 0 \le t \le T, \\ 1 & , \quad t > T, \end{cases}$$

where $T = 2\pi / \omega$, $A(t)$ is the amplitude, $\varepsilon = 0.00573$. The other flow parameters in the oscillator region are calculated as for the case of a wall without an oscillator. The perturbation with frequency $\omega_0^* / 2\pi = f_0^* = 6.36$ kHz and wave number $\beta_0^* = 211.52$ m^{-1} will be referred to as a fundamental perturbation.

As will be shown below, the results of the present calculations are in good agreement with the results of [1, 2] both qualitatively and quantitatively. However, the perturbation amplitude in the present paper and in paper [1] differs from the amplitude from paper [2] by nearly half (in paper [2] $\varepsilon = 0.003$) and is chosen to coincide with the position of origin of LTT (in [1] it is shown that the numerical dissipation does not affect the LTT position, and it is assumed that in paper [2] the perturbation amplitude is given wrongly).

2.6 Computational grid

The characteristic length scale is chosen as $L = 0.7239$м. The longitudinal size of the buffer zone, which is bounded by the dashed rectangle in Figure 5, is one and a half wavelengths of the fundamental perturbation, or $1.5\lambda_x$ where $\lambda_x = x_2^* - x_1^*$. In the present paper the computational meshes from [1] are used.

Figure 5 shows the calculation area and calculation grid (side view). The sub-area for the basic non-stationary calculations is bounded by a solid rectangle and begins at a distance of $x_0^* = 0.258$ m from the leading edge of the plate. The sub-area length is 14.3 times the longitudinal wavelength of the fundamental perturbation. The height of the subarea is chosen to be $y_H^* = 0.03$ m, which is no less than five local thicknesses of the boundary layer at the output boundary. The size of the sub-area in the lateral direction is one wavelength λ_z in the transverse direction, where $\lambda_z = 2\pi / \beta_0^* \approx 0.0297$ m.

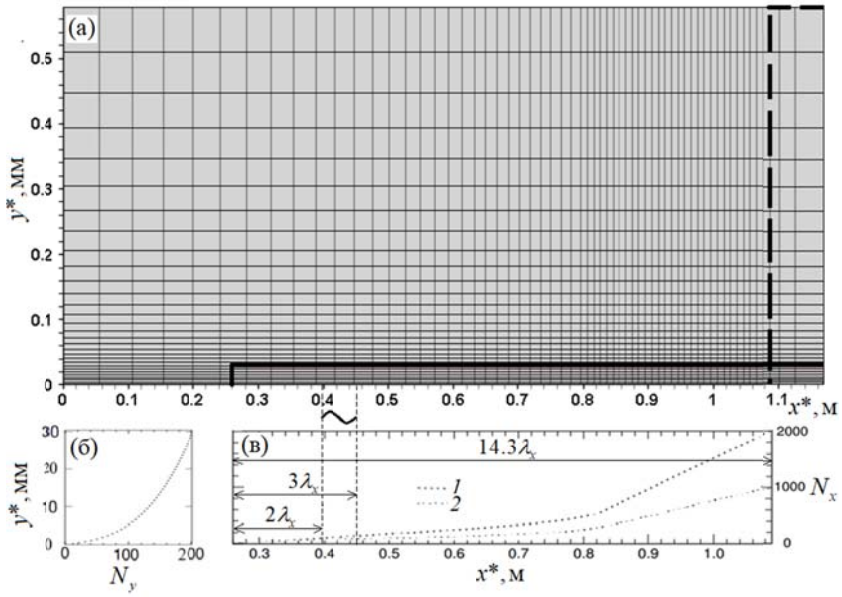

Figure 5 - Computational mesh parameters: (a) general view (every 10th grid line is shown); (b) grid clustering along the normal to the wall; (c) grid clustering in longitudinal direction: 1 - 80 million grid nodes, 2 - 20 million grid nodes.

The computational grid is shown in Figure 5a, the corresponding grid densifications in Figs. 5b and 5c. The main calculations of the present work were performed on a grid of 80 million nodes (detailed grid). This grid corresponds to the grid from work [2] in the plane xOy. The mesh lines are distributed uniformly in transverse direction. The number of points along the axis is 201 on the detailed grid. The coarse mesh has half the number of nodes along x and along z, than the detailed mesh. In the vertical direction, the number of points is the same for both grids; there are at least 100 points across the boundary layer. On the detailed grid the fundamental perturbation is resolved in the lateral direction (by z) by 201 points per wavelength by z, and in the longitudinal direction (by *x*) by 320 points. It is worth noting that the propagation of a monochromatic acoustic wave in a uniform flow requires about 40 points per wavelength to achieve close to the natural level of viscous wave attenuation for the dissipative numerical method used. Therefore the numerical dissipation of the fundamental perturbation is negligible on the meshes constructed. It can be assumed that perturbations with a wavelength four times shorter than the fundamental wavelength are modelled quite reliably, which allows one to "capture" the laminar-turbulent

2.7. Quantities analysed

Data for processing and comparison are collected starting from the moment of dimensionless time $t = 2.261$ after the perturbation is introduced into the boundary layer, when a quasi-periodic flow regime is established. In the next section, the properties of the transient flow are analysed.

The analysis is performed for the spectral composition of disturbances where the amplitudes of individual Fourier harmonics or the maxima of these amplitudes along the surface normal in the considered cross section $x = const$ are compared. The Fourier analysis and processing of non-stationary results is performed using the capabilities of the Python programming language (numpy library). The results of the fast Fourier transform procedures for time and coordinate z are normalized to $N_t \times N_z / 4$, where N_t and N_z are the number of points of the analyzed signal for time and coordinate z, respectively. In the present paper the amplitudes of harmonics of pulsations of longitudinal component of velocity, pressure, temperature, and maximums of these values along the surface normal are investigated.

The vortex structure of the flow fields is visualized using the Q-criterion: $Q = 0.5(\Omega_{ij}\Omega_{ij} - S_{ij}S_{ij})$, $S_{ij} = 0.5(\partial_j u_i + \partial_i u_j)$, $\Omega_{ij} = 0.5(\partial_j u_i - \partial_i u_j)$, u_i are the velocity vector components (tensor notation is used for the record; agreement on summation by a repeated index in the product is assumed) [7].

The fields of instantaneous values of longitudinal and transverse components of the eddy vector and average flow parameters (friction coefficient, Favre and Reynolds averaged profiles of

longitudinal velocity components) are also compared.

3. Analysis of results

3.1 Flow structures

The instantaneous structure of the perturbed flow is represented in Figure 6 as isosurfaces-criteria. Immediately behind the source of perturbations is a region of linear development of perturbations, where they form X-shaped structures that intensify downstream. Nearby $x^* \approx 0.6$ мм there are the first signs of a nonlinear interaction - perturbations begin to distort. At $x^* \in (0.75, 0.85)$ m there is intense nonlinear perturbation decay. Beyond this region, a young turbulence zone forms with the growth of small-scale vortices. This zone develops downstream. It can be seen that for the hybrid scheme (the present work) the size of the resolved fine-scale vortices is smaller than in the case of the monotonic scheme (work [1]). This difference is observed in the nonlinear regime region at $x^* > 0.85$ m.

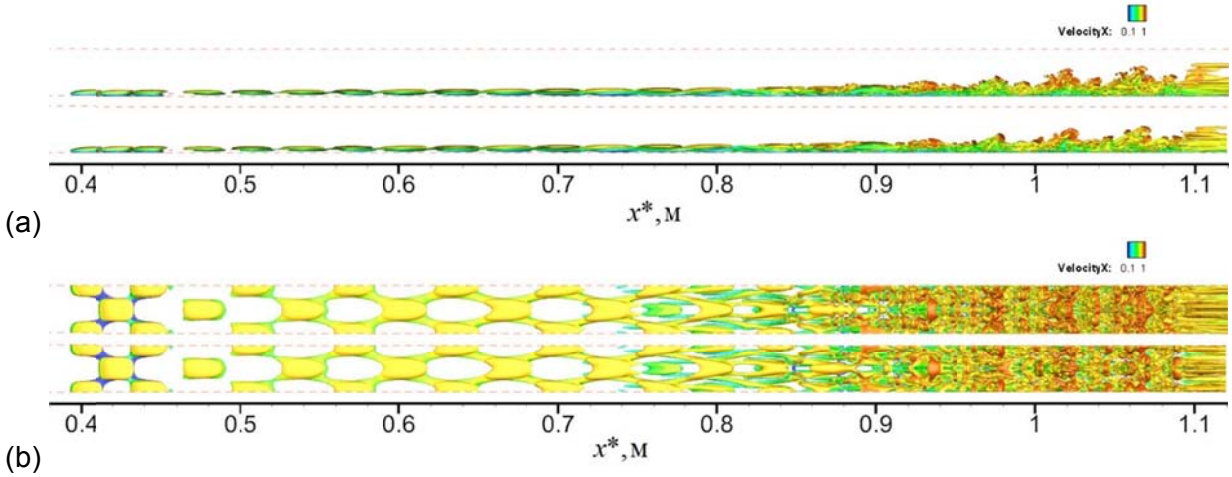

Figure 6 - Visualization of the vortex structures of the boundary layer using Q-criterion isosurfaces, $Q = 5$, 20 million node grid, top - is the present paper, bottom - paper [1]: (a) side view from $+z$; (b) top view from side $+y$. The coloring corresponds to the magnitude of the longitudinal component of the velocity vector. The buffer zone starts at $x^* \approx 1.09$ m.

Since the excitatory perturbations are periodic with a dedicated frequency and nonlinear interactions generate multiple harmonics, the boundary layer response to such perturbations remains periodic (quasi-stationary flow regime). In order to study the spectral properties of the LTT process, the unsteady flow is first set up to a quasi-stationary regime and then statistics are gathered for five time periods of the fundamental perturbation.

At each cross section $x^* = const$ the perturbation can be represented through a sum of harmonic oscillations by means of a Fourier transform. For the considered flow along the plane plate it is reasonable to perform a two dimensional Fourier transform in time and transverse coordinate for each line $x^* = const$, $y^* = const$. The result of such a two dimensional transformation can be represented as the amplitude of harmonic $(f^*, \beta^*) = (hf_0^*, k\beta_0^*)$. Thus the result of the two dimensional Fourier transform can be represented as the amplitudes of the two dimensional harmonics $\hat{u}_{hk}$. An example is shown in Figure 7 for the beginning of the young turbulence region.

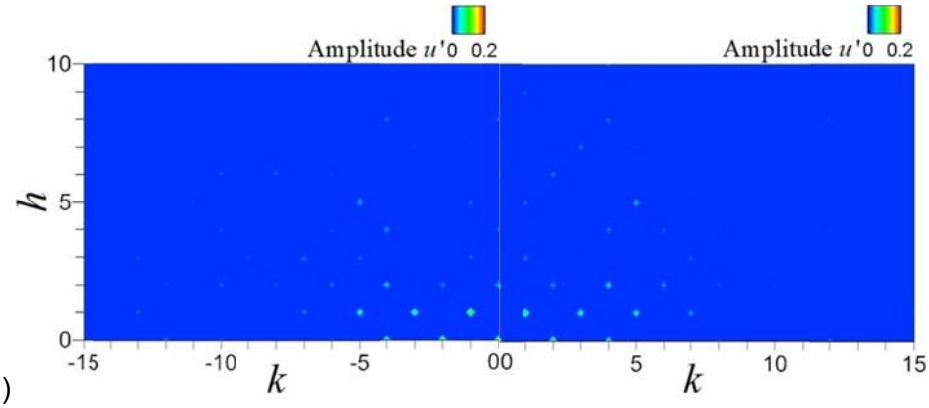

(a) (б)

Figure 7 - Two-dimensional Fourier transform of the field $u'(t, x_0^*, y_0^*, z)$ on line $(x_0^*, y_0^*) = (0.9201, 0.0035)$ m, grid of 80 million nodes: (a) work [1], (b) present work.

In the described formulation the Fourier spectrum is symmetric, so only part of the spectrum at $h \geq 0$, $k \geq 0$. It should be noted that the spectrum peaks are staggered, which is explained by a quadratic (nonlinear) interaction of perturbations with each other. For example, for a stationary perturbation and other even frequencies $h = 0, 2, 4, \ldots$ only maxima at even wave numbers $k = 0, 2, 4, 6, \ldots$ are observed, while for odd frequencies $h = 1, 3, 5, \ldots$ the maxima are observed at odd wave numbers $h = 1, 3, 5, \ldots$. Such picture is characteristic for the slanted decay mechanism when two harmonics with identical frequencies but opposite in sign wave numbers interact nonlinearly (quadratically). At the same time, the frequency doubles and the wave number is zeroed out $[1,1] + [1,-1] \rightarrow [2,0]$. The closer the harmonic is to the fundamental harmonic, the higher its amplitude. This is due both to the fact that the nonlinear decay advances gradually to higher frequencies and that there is a numerical space-time dissipation of the numerical method used. Calculations of the present work are performed on two different meshes, one of which is twice as shallow in the longitudinal and lateral directions. From Figure 7a and 7b show that the perturbation spectrum obtained using the hybrid scheme appears to be somewhat broader than in the case of the monotonic scheme.
Below obtained results are compared with the results of [1] and [2].

3.2 Linear regime

Consider the linear mode of perturbation development which is observed approximately from $x^* = 0.4$ m to $x^* = 0.6$ m. In Figure 8 the amplitudes of the fundamental mode $[1,1]$ of the longitudinal velocity vectorpulsations u' in cross section $x^* = 0.5$ m obtained in the present work are compared with the results of [1] and [2]. For this case and for other lines $x^* = const, y^* = const$, good agreement is observed (Figs. 8a-c).
Among all possible lines $y^* = const$ for the given section $y^* = const$ one can distinguish the line y_0^*, on which the amplitude of the harmonic in question is maximal. For pulsations u' or T' this line will be in the critical layer of the boundary layer $y_0 / \delta \approx 0.65$.

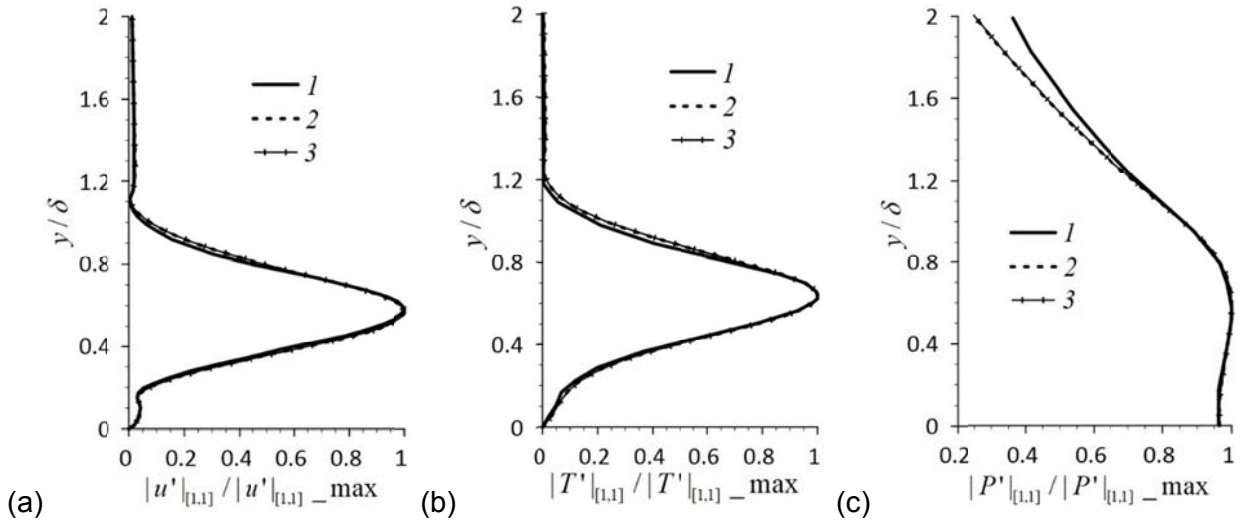

Figure 8 - Harmonic amplitudes [1, 1] on a grid of 80 million nodes in section $x^* = 0.5$ m: (a) $|u'_{[1,1]}|$, (b) $|T'_{[1,1]}|$, (c) $|p'_{[1,1]}|$. 1 - work [2], 2 - work [1], 3 - present work.

Compared to the monotonic scheme of [1] the hybrid scheme of the present paper gives almost identical solutions. This means that in the linear regime the dissipative component has very little effect on the detailed grid solution.

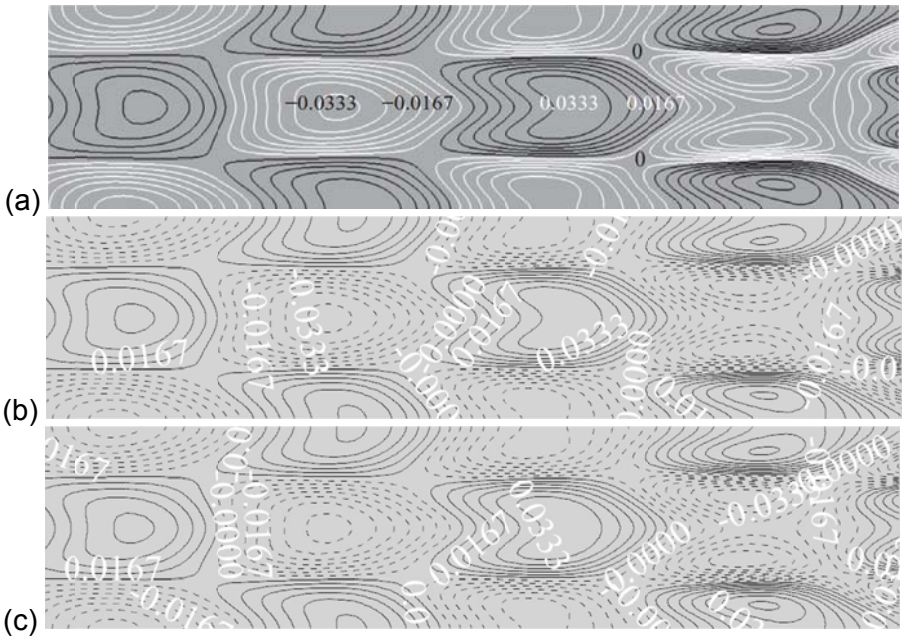

Figure 9 - Instantaneous pulsation u' contour for section $x^* = 0.546...0.67$ m on a grid of 80 million nodes, $y^* = 2.3$ mm: (a) work [2], (b) work [1], (c) present work.

Figure 9 shows the perturbation patterns within the boundary layer at cross section $y^* = const$. All fields are in good agreement with each other. The hybrid scheme gives slightly more filled contours compared to the monotonic scheme and agrees better with [2], but this difference is insignificant.

3.3 Nonlinear regime

Let us consider the nonlinear stage of perturbation development. The moment of manifestation of the nonlinear interaction can be noted from the Q-criterion patterns, in which the amplification of "rope-like" structures (Figs. 10 and 11) is noticeable. For small values (15 and 100) (Figure 10) on a grid of 20 and 80 million nodes, the hybrid and monotonic schemes yield almost identical structures of Q values. They agree well with the results of [2].

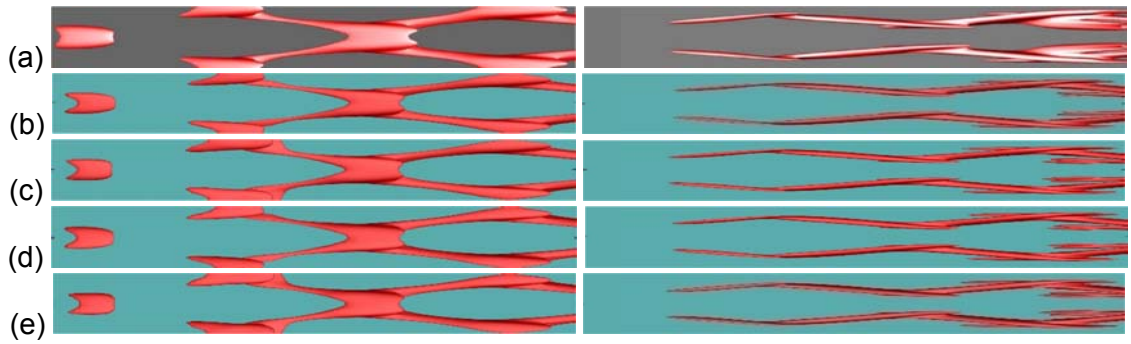

Figure 10 - Q-criterion instantaneous isosurfaces, top view; left - Q = 15, x* = 0.546 - 0.670 m, right - Q = 100, x* = 0.670 - 0.798 m: (a) work [2] on a grid of 80 million nodes, (b) work [1] on a grid of 20 million nodes, (c) work [1] on a grid of 80 million nodes, (d) present work on a grid of 20 million nodes, (e) present work on a grid of 80 million.

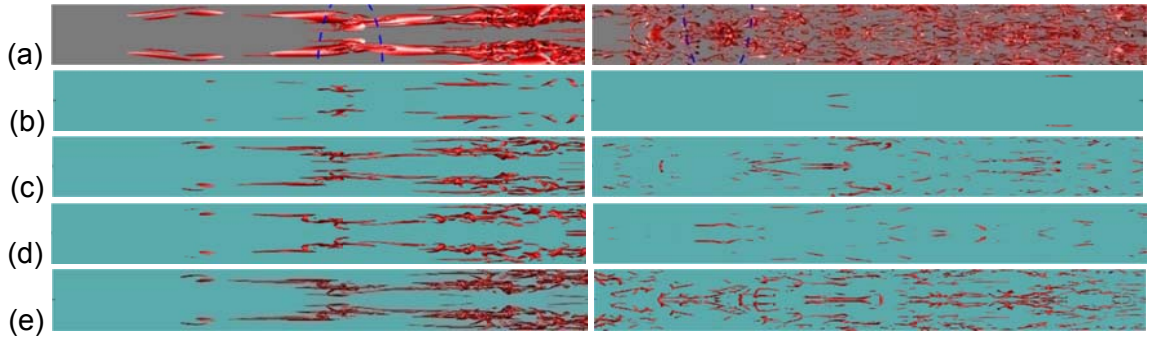

Figure 11 - Q-criterion instantaneous isosurfaces, top view; left - Q = 10000, x* = 0.798 - 0.924 m, right - Q = 40000, x* = 0.924 - 1.051 m: (a) work [2] on a grid of 80 million nodes, (b) work [1] on a grid of 20 million nodes, (c) work [1] on a grid of 80 million nodes, (d) present work on a grid of 20 million nodes, (e) present work on a grid of 80 million.

However, in the region of young turbulence, where fine-scale structures appear and the maximum magnitude increases (10000 and 40000) (Figure 11), the dissipative scheme does not perfectly reproduce the results of the low-dissipative scheme [2]. The most probable reason of this discrepancy is application in [2] spectral method in lateral direction and using of high-frequency harmonics which are situated near Nyquist frequency (wave number) for detailed calculation grid of the present paper and therefore are badly resolved on it.

The fullness of the vortex structures obtained using the hybrid scheme on the coarse grid (Figure 11c) corresponds well to the case of the detailed grid (Figure 11c, d) for both the monotonic and hybrid schemes. However, the corresponding structures obtained on the original monotonic scheme on the coarse grid turn out to be much weaker (Figure 11b). Therefore, it can be concluded that, on the coarse grid, the hybrid scheme gives more plausible results than the monotone scheme.

The above conclusion is confirmed quantitatively by means of the evolution of the amplitudes of individual harmonics. Let us consider in particular the evolution of the maximum in *y* direction amplitudes. The oblique resonance mechanism appears sequentially. Initially, the most unstable fundamental oblique wave $[1,\pm 1]$ grows due to a purely unstable boundary layer. At some critical amplitude it begins to nonlinearly interact with itself, generating multiples: $h=0$ and $h=2$, $k=0$, $k=2$, which begin to grow due to nonlinear interaction of the fundamental harmonics. When the multiples reach sufficient amplitudes, they begin to non-linearly interact with each other and with the fundamental harmonics, generating more and more multiples. Such process and its time sequence can be traced on Figure 12 and Figure 13, where the evolution of harmonic amplitudes down stream is shown. The described mechanism explains the staggered structure of the spectrum in Figure 7.

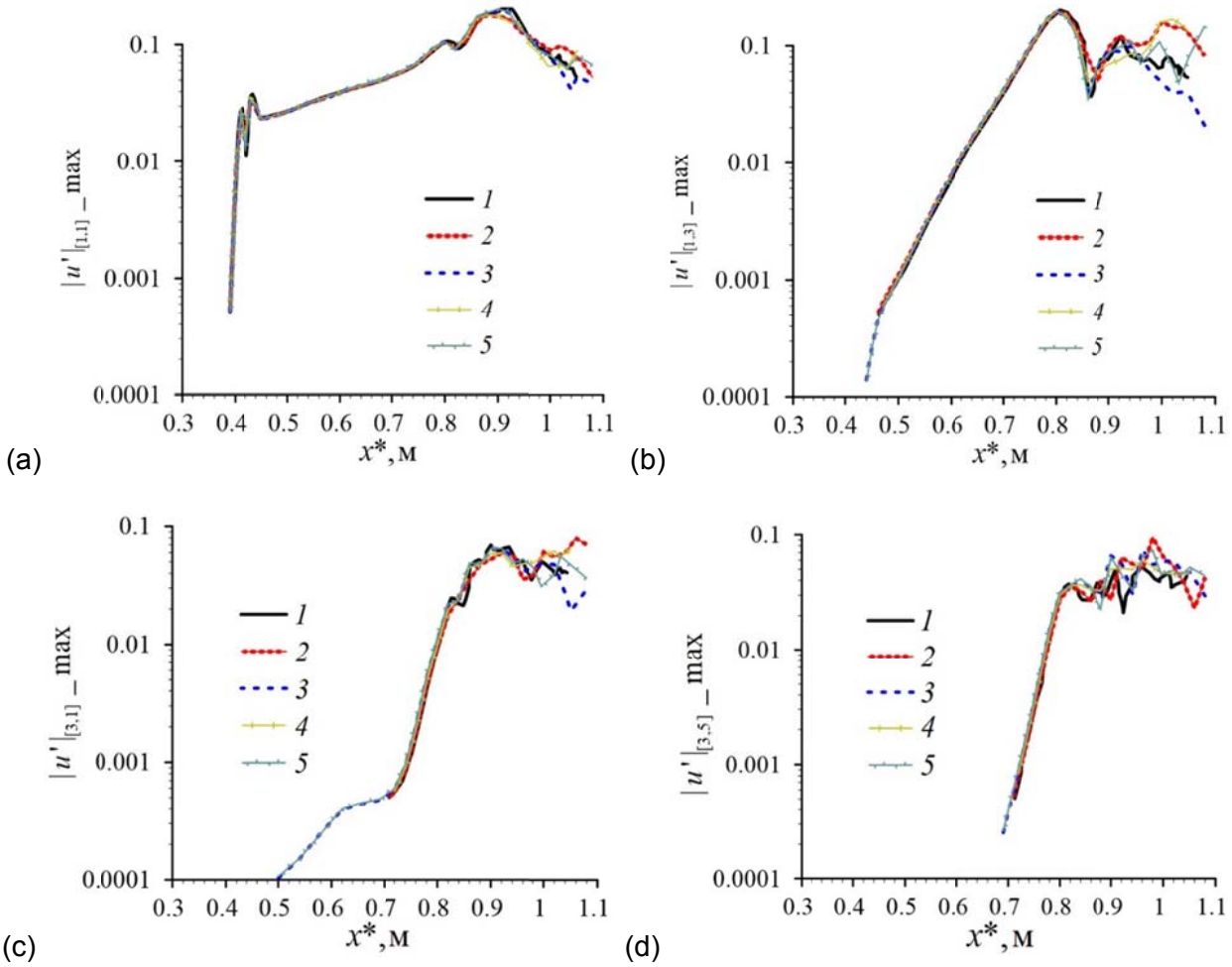

Figure 12 - Evolution of the maximum in *y* amplitude Fourier-harmonic for odd frequencies, 1 - work [2] on a grid of 80 million nodes, 2 - work [1] on a grid of 20 million nodes, 3 - work [1] on a grid of 80 million nodes, 4 - present work on a grid of 20 million nodes, 5 - present work on an 80 million node grid: (a) $[h,k]=[1,1]$, (b) $[h,k]=[1,3]$, (c) $[h,k]=[3,1]$, (d) $[h,k]=[3,5]$.

Figure 12a shows the evolution of the fundamental mode of the longitudinal velocity component obtained on a grid of 80 million nodes using the hybrid scheme (line 5). The solution is closer to that of [2] than in the case of the monotonic scheme [1] (line 3). On a 20 million node grid, the solution using the hybrid scheme (line 4) is also similarly closer to [2] and almost reaches before the solution using the monotonic scheme and the 80 million node grid (line 3). In Figure 12b-d the difference in the lines is not as clear.

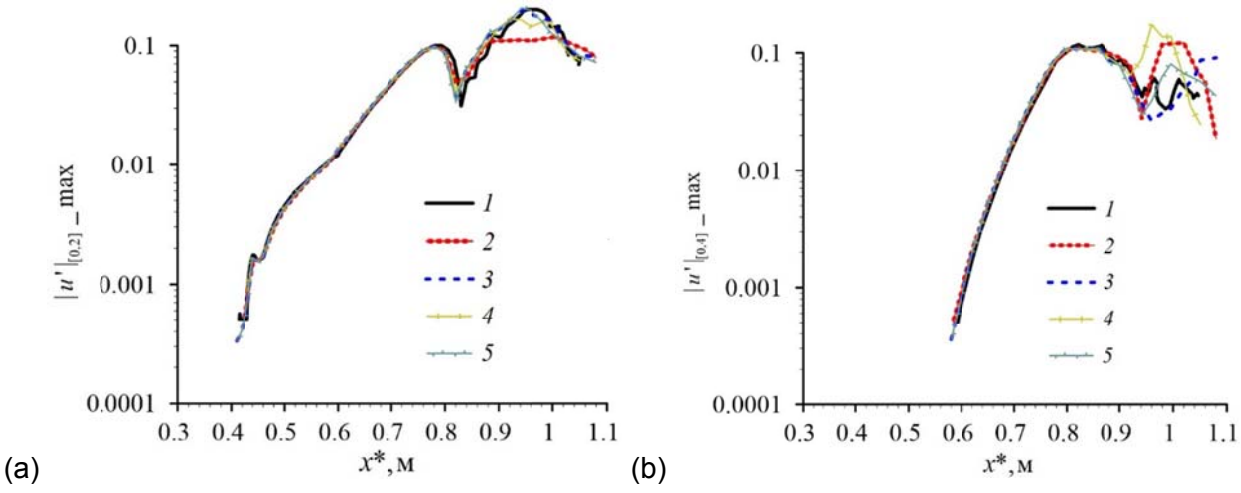

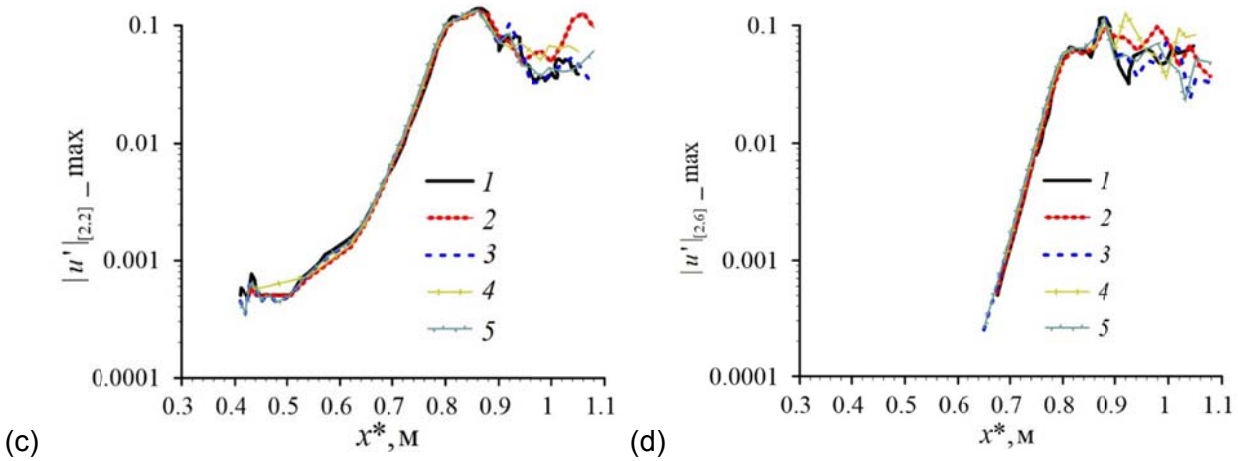

Figure 13 - Same as Figure 12, but for even frequencies: (a) $[h,k]=[0,2]$, (b) $[h,k]=[0,4]$, (c) $[h,k]=[2,2]$, (d) $[h,k]=[2,6]$.

Figure 13a demonstrates that on a 20 million node grid, the monotonic scheme solution (line 2) is very different from the solution [2]. However, the solution obtained using the hybrid scheme (line 4) matches the monotonic scheme solution on a grid of 80 million nodes much better (line 3). In Figure 13b-d the line differences are fuzzy.

Thus, the hybrid scheme gives solutions that agree better with the solution [2] compared to the case of the monotonic scheme [1]. On a coarse mesh, the solution of the hybrid scheme can reach the accuracy of the solution of the monotonic scheme on a fine mesh. The differences in the solutions using monotonic and hybrid schemes are more pronounced in the low modes.

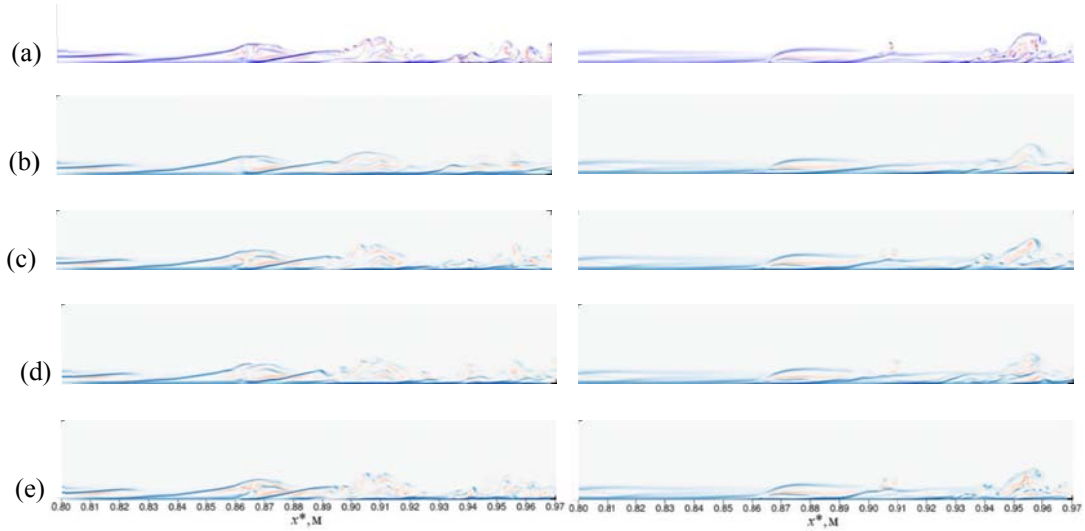

Figure 14 - Instantaneous field of the transverse eddy vector at time t = 2.82891+kT, left - z* = -0.0062m, right - z* = -0.0032m: (a) work [2] on a grid of 80 million nodes, (b) work [1] on a grid of 20 million nodes, (c) work [1] on a grid of 80 million nodes, (d) present work on a grid of 20 million nodes, (e) present work on a grid of 80 million nodes.

Figure 14 shows the instantaneous structures of transverse vector of turbulence in different cross sections $z^* = const$ and comparison of the obtained results with the results of [1] and [2]. It can be seen that small-scale structures typical of developed turbulence appear in the vicinity of $x^* = 0.865$ m. The main large-scale structures of this paper and paper [1] agree well with [2]. A detailed comparison shows that the vortices obtained in Paper [1] are less intense compared to those in

Paper [2] and contain fewer fine-scale structures, as discussed above. However, the hybrid scheme of the present work resolves the vortex structures better (Figure 14d, e) than the monotonic scheme [1] (Figure 14b, c). Visually, the hybrid scheme achieves detailed grid accuracy using a coarse mesh [2].

Figure 15 shows instantaneous cross sections of the longitudinal component of the swirl vector, which are compared with the results of [1] and [2]. The flow pattern is symmetrical with respect to the z*=0 plane; therefore only half of the z* region is shown. There is a large vortex in the cross section (Figure 15a). As *x* increases it grows and, starting from $x^* = 0.872\text{M}$ (Figure 15b), it disintegrates to form smaller vortices. The results obtained for the hybrid scheme (the present work) agree better with the results of [2] for the monotonic scheme (work [1]).

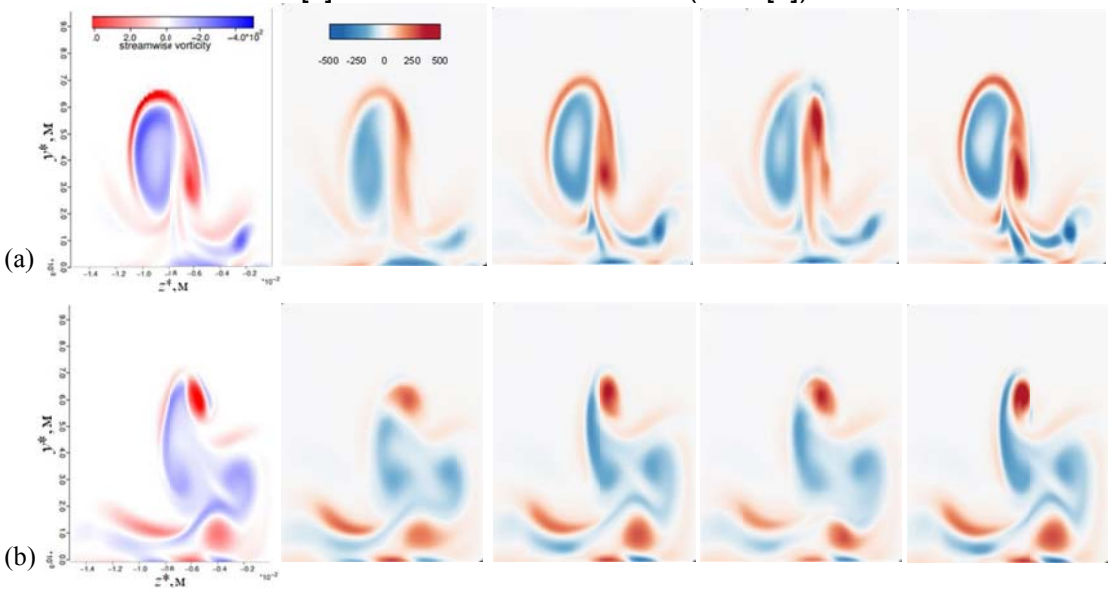

Figure 15 - Instantaneous longitudinal vector of swirl at time t = 2.82891+kT, from left to right work [2] on grid of 80 million nodes, work [1] on grid of 20 million nodes, work [1] on grid of 80 million nodes, present work on grid of 20 million nodes, present work on grid of 80 million nodes respectively: (a) x* = 0.862 m, (b) x* = 0.870 m.

Consider the dependence of the averaged value of the friction coefficient c_f on the longitudinal coordinate *x*. The local friction coefficient is calculated using the formula

$$c_f = \frac{2}{\mathrm{Re}_\infty} \times \mu \Big| \times \frac{\partial u}{\partial y}\Big|_{y=0} .$$

As in [1], the present paper considers time averaging over five periods of the fundamental harmonic $\Delta t = 10\pi / \omega_0$ and over the z-span of the entire computational domain:

$$\overline{\varphi} = \frac{1}{\lambda_z}\frac{1}{\Delta t}\int_0^{\lambda_z}\int_{t_0}^{t_0+\Delta t} \varphi(t,z)\,dtdz .$$

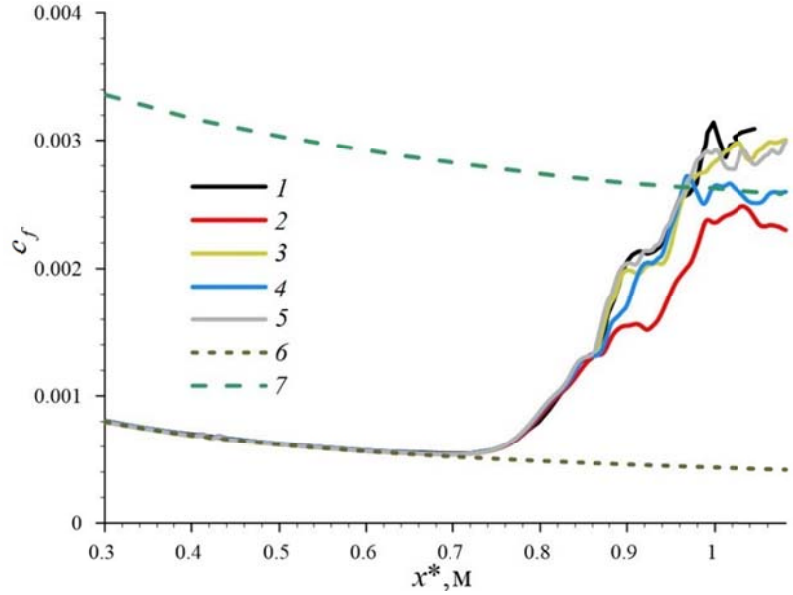

Figure 16 - Space and time averaged friction coefficient: 1 - work [2] on a grid of 80 million nodes, 2 - work [1] on a grid of 20 million nodes, 3 - work [1] on a grid of 80 million nodes, 4 - present work on a grid of 20 million nodes, 5 - present work on a grid of 80 million nodes, 6 - laminar branch, 7 - theoretical turbulent branch [8].

Starting from $x^* = 0.72\,\text{м}$, the magnitude c_f increases sharply in the vicinity of the point $x^* = 0.86\,\text{м}$ - in the region of the onset of transition to turbulence. In this range the results for dissipative and hybrid schemes coincide with the results of [2] even on coarse grid. Downstream, the results on the coarse grid are lower compared to the detailed grid case. This is particularly evident for the monotonic scheme, while in the case of the hybrid scheme the corresponding curve deviates little from the case of the detailed computational mesh $(x^* \geq 0.9\text{м})$.

Figure 17 shows the average profiles of the gas dynamic variables in cross section $x^* = 0.996\,\text{м}$. The stronger the effect of nonlinear interactions in the cross section in question, the more crowded the average profiles are.

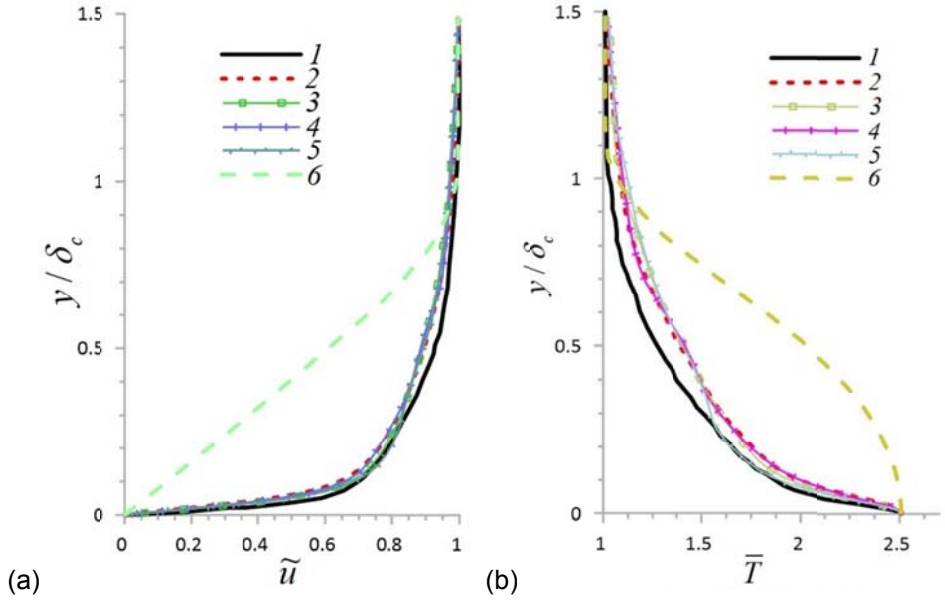

Figure 17 - Favre averaging of longitudinal velocity (a) and Reynolds averaging of temperature (b) in section x*=0.996 m: 1 - work [2] on a grid of 80 million nodes, 2 - work [1] on a grid of 20 million nodes, 3 - work [1] on a grid of 80 million nodes, 4 - present work on a grid of 20 million nodes, 5 - present work on a grid of 80 million nodes, 6 - laminar branch.

Figure 17 confirms that in spite of insufficiently detailed picture of small-scale vortices obtained with

dissipative method [1], integral characteristics of the flow (average profiles of gas-dynamic variables, average friction coefficient) appear to be quite close to the results obtained with low-dissipative schemes [2]. At the same time, the hybrid scheme of the present work gives better results even on a coarse grid. This conclusion is important for applied problems where it is not necessary to solve in detail all structures of the developed turbulent motion, but it is required to obtain reliable integral characteristics of the flow. For such problems, the application of the hybrid scheme on a coarse grid allows to obtain satisfactory results with limited computational resources.

4. Conclusions

A hybrid difference scheme for modelling the development of perturbations in supersonic boundary layers has been proposed. The scheme is based on a smooth solution indicator and allows one to smoothly reduce the dissipation of the original monotonic scheme with respect to the convective flow quantities by reducing the monotonic correction that occurs when solving the Riemann problem. The reduction is possible up to some threshold value. With further reductions, the scheme seems to lose stability. It is empirically established that the threshold level of the monotonic correction depends on the quality of the mesh and the intensity of the external perturbations.

The perturbation evolution calculated using the hybrid scheme on the coarse computational mesh agrees well with the results of other works, including those obtained on the detailed mesh using the monotonic scheme. However, the monotonic scheme on the coarse grid underestimates the perturbations and resolves the small-scale vortex structures in the region of young turbulence much worse than the case of the hybrid scheme.

The proposed hybrid difference scheme is suitable for modelling the development of non-stationary perturbations in supersonic boundary layers. It allows one to obtain satisfactory results on limited computational resources.

This work was carried out with financial support from the Russian Science Foundation (project code 21-19-00307) at MIPT using the equipment of the "Modelling and Data Processing Complex for Mega-Class Research Facilities" of NRC Kurchatov Institute, http://ckp.nrcki.ru/.

5. Contact Author Email Address

mailto: nguyennhucan528@gmail.com

6. Copyright Statement

References

[1] Egorov I.V., Nguyen Can, Nguyen T., Chuvakhov P.V. Simulation of laminar-turbulent transition with dissipative numerical scheme application. *Computational Mathematics and Mathematical Physics*, Vol. 61, No. 2, 2021.

[2] Mayer C.S.J., Terzi D.A.V., Fasel H.F. DNS of Complete Transition to Turbulence Via Oblique Breakdown at Mach 3. *AIAA*, 2008-4398, 2008.

[3] Egorov I.V., Novikov A.V. Direct numerical simulation of laminar–turbulent flow over a flat plate at hypersonic flow speeds. *Computational Mathematics and Mathematical Physics*, Vol. 56, No. 6, pp 1048-1064, 2016.

[4] Ducros F. et.al. Large-Eddy Simulation of the Shock / Turbulence Interation. *Journal of Computational Physics*, Volume 152, Issue 2. 1, Pages 517-549, July 1999.

[5] Bashkin V.A., Egorov I.V. *Numerical Simulation of Viscous Perfect Gas Dynamics*. New York • Connecticut: Begell House Inc., 2016.

[6] Chuvakhov P.V., Fedorov A.V. & Obraz A.O. Numerical simulation of turbulent spots generated by unstable wave packets in a hypersonic boundary layer. *Computers & Fluids*, Vol. 162, pp 26–38, 2018 Available at: http://dx.doi.org/10.1016/j.compfluid.2017.12.001

[7] Vyshinsky V.V., Sizykh G.B. The verification of the calculation of stationary subsonic flows and the presentation of the results. *Mathematical Models and Computer Simulations,* Vol. 11, No. 1, pp 97–106, 2019.

[8] White F. M. *Viscous Fluid Flow*. New York: McGraw-Hill, 1991.